

## Near-neighbor mixing and bond dilation in mechanically alloyed Cu-Fe

V. G. Harris, K. M. Kemner, B. N. Das, N. C. Koon, and A. E. Ehrlich  
*U.S. Naval Research Laboratory, Washington, D.C. 20375*

J. P. Kirkland  
*SFA Inc., Landover, Maryland 20785*

J. C. Woicik  
*National Institute of Standards and Technology, Gaithersburg, Maryland 20899*

P. Crespo and A. Hernando  
*Instituto de Magnetismo Aplicado, Las Rozas, 28230 Madrid, Spain*

A. Garcia Escorial  
*Centro Nacional de Investigaciones Metalurgicas—Centro Superior de Investigaciones Cientificas, 28040 Madrid, Spain*  
(Received 5 January 1996; revised manuscript received 4 April 1996)

Extended x-ray-absorption fine-structure (EXAFS) measurements were used to obtain element-specific, structural, and chemical information of the local environments around Cu and Fe atoms in high-energy ball-milled  $\text{Cu}_x\text{Fe}_{1-x}$  samples ( $x=0.50$  and  $0.70$ ). Analysis of the EXAFS data shows both Fe and Cu atoms reside in face-centered-cubic sites where the first coordination sphere consists of a mixture of Fe and Cu atoms in a ratio which reflects the as-prepared stoichiometry. The measured bond distances indicate a dilation in the bonds between unlike neighbors which accounts for the lattice expansion measured by x-ray diffraction. These results indicate that metastable alloys having a positive heat of mixing can be prepared via the high-energy ball-milling process. [S0163-1829(96)10033-3]

### I. INTRODUCTION

In recent years there has been renewed interest in extending the mutual solubility of Fe and Cu. One reason is the observation of giant magnetoresistance in heterogeneous samples which have small ferromagnetic particles coherently suspended within a nonmagnetic noble metal matrix.<sup>1,2</sup> The easiest way to obtain such a structure in the Cu-Fe system is the controlled heat treatment of a solid solution. However, obtaining a solid-solution of Cu-Fe is not a trivial matter. The Cu-Fe equilibrium phase diagram indicates little or no miscibility of either constituent at room temperature, and only  $\approx 4$  at. % Fe dissolves into Cu and  $\approx 10$  at. % Cu into Fe near their respective liquidus lines.<sup>3</sup> However, extended regions of metastable solubility can be obtained via vapor-quenching techniques.<sup>4,5</sup> Recently, an alternative path to vapor-quenching, high-energy ball-milling (HEBM), has been proposed to form solid solutions of combinations of elements having a positive heat of mixing.

HEBM is a process which utilizes the energy of ballistic collisions between particles of a charge material and the surface of hardened steel balls and/or the walls of a shaking container to mix, fragment, and ultimately amorphize or dissolve the charge materials. HEBM has become a popular technique in recent years for the solid-state amorphization of binary metal systems,<sup>6,7</sup> metal-metalloid systems,<sup>8-10</sup> and even single-component systems.<sup>11</sup> Thermodynamic and kinetic models which explain these processes have been proposed.<sup>12-15</sup> It had been widely held that a negative heat of mixing was required in order to experience single-phase, atomic mixing (i.e., alloying) in the HEBM binary metal systems. However, recently HEBM has been reported to

form metastable alloys, or more correctly supersaturated solid solutions, of combinations of elements which do not exhibit appreciable solubility in their equilibrium phase diagrams.<sup>15-21</sup> The alloying phenomenon in these materials has been explained by Yavari, Desre, and Benameur<sup>15</sup> to arise when small fragments, created by codeformation, obtain a critical tip radii, whereupon capillary forces bring about the dissolution of the tip region. Subsequently, the solute content changes within the local spinode increasing the critical radius causing the more rapid dissolution of the region and the eventual complete mixing of one component into the other.

The reports concerning the formation and characterization of HEBM alloys having a positive heat of mixing have relied largely upon electron microscopy and x-ray-scattering techniques to establish the onset and degree of mixing. However, when crystallites become increasingly strained and reduced in size, as they do in HEBM, diffracted intensities experience a reduction in amplitude from Debye-Scherrer broadening, leading to the smearing of the diffraction features often beyond visual detection. These effects may lead to a misinterpretation of these data and consequently a misunderstanding of the physical state of the sample.

In order to investigate if alloying occurs in HEBM samples having a positive heat of mixing, we have used x-ray diffraction in combination with extended x-ray-absorption fine-structure (EXAFS) measurements to study both the long-range and the short-range structure and chemistry in HEBM  $\text{Cu}_x\text{Fe}_{1-x}$  ( $x=0.5$  and  $0.7$ ) samples. These compositions are well outside the miscibility regions in the Cu-Fe equilibrium phase diagram and are not expected to form solid solutions under steady-state conditions.

The magnetic and structural properties of HEBM Cu-Fe samples, including those having the same compositions as studied here, have been reported previously by others.<sup>15,22–26</sup> In those studies, the degree of chemical and structural short-range order was indirectly measured using magnetic measurements, x-ray diffraction, and/or thermal analysis. In an earlier study, Harris *et al.* employed EXAFS to study HEBM Cu<sub>70</sub>Fe<sub>30</sub>, Ag<sub>70</sub>Co<sub>30</sub>, and Ag<sub>70</sub>Fe<sub>30</sub> samples and found via EXAFS near-neighbor modeling analysis that atomic-level mixing had occurred in the Cu<sub>70</sub>Fe<sub>30</sub> sample which had been milled for 20 h, but not in the Ag-based samples, even after 200 h of milling.<sup>19</sup> Crespo *et al.*<sup>20</sup> reported the results of EXAFS measurements on HEBM Cu<sub>50</sub>Fe<sub>50</sub> samples that indicated the nearest-neighbor coordination sphere did indeed reflect a mixed chemistry very near to the nominal values of the starting materials indicating the existence of a supersaturated solid solution. Recently, Schilling *et al.*<sup>21</sup> used EXAFS to study the local environments of ball-milled Cu<sub>50</sub>Fe<sub>50</sub> and Ag<sub>50</sub>Fe<sub>50</sub> samples and similarly found that the Cu<sub>50</sub>Fe<sub>50</sub> samples alloyed, while the Ag<sub>50</sub>Fe<sub>50</sub> samples did not.

In this work we provide direct structural evidence that both the Fe and Cu atoms reside in the fcc lattice with a near-neighbor chemistry very near the nominal stoichiometry of the starting materials. These results establish the absence of fcc or bcc single-element clusters, coherent or incoherent, within these samples and indicate that atomic-level mixing has indeed taken place via the HEBM process. In addition, a dilation of the bonds between unlike neighbors was measured via EXAFS which accounts for the expansion of the lattice observed in x-ray-diffraction measurements. This dilation is unique to the unlike atom pairs and is not observed in the bonds between like atom pairs.

## II. MISCIBILITY, ELECTRONIC, AND MAGNETIC PROPERTIES OF Cu-Fe

### A. Miscibility

The Cu-Fe equilibrium phase diagram indicates limited solubility of each element into the other. The solubility of Fe into Cu is about  $\approx 4$  at. % at the melting point (1094 °C) and decreases to 0.1 at. % at 600 °C, and to even smaller amounts near room temperature, while the solubility of Cu into Fe is a maximum  $\approx 10$  at. % at 1477 °C and remains constants at  $\approx 0.5$  at. % near room temperature.<sup>3</sup> Studying dilute solid solutions, researchers found each element to expand the lattice of the other.<sup>27</sup> However, several research groups have explored a variety of rapid-quenching techniques which extend the room-temperature miscibility regions by forming metastable alloy concentrations.

The first experimental work on extending the miscibility of the Cu-Fe system was performed on bulk solid samples rapidly quenched from elevated temperatures.<sup>28,29</sup> These studies were successful in stabilizing up to 15 at. % of Cu in the bcc Fe matrix. The measured lattice parameters of these alloys were shown to increase near linearly with Cu content following Vegard's law. Anneals at 573–873 K were reported to facilitate the decomposition of the alloys to nearly pure bcc Fe and fcc Cu components.

Using liquid quenching, Klement further extended the miscibility of Cu into bcc Fe to 17.5 at. % and Fe in fcc Cu to 20 at. %.<sup>30</sup> These authors found compositions between these two limits to exist as heterogeneous mixtures of bcc

and fcc phases. With the development of vapor-quenching techniques the miscibility regions were significantly extended. Kneller,<sup>31</sup> using thermal evaporation, found Fe-Cu alloys having up to 50 at. % Cu to have a bcc structure, while alloys with more than 70 at. %, Cu could be stabilized in the fcc structure. Once again, intermediate compositions were reported to consist of mixtures of the two phases. Sumiyama, Yoshitake, and Nakamura,<sup>4</sup> using rf sputter deposition, further extended the miscibility of Cu in bcc Fe and Fe in fcc Cu to nearly 45 at. % of each. The extended miscibility experienced in sputter deposition over that of thermal evaporation is presumably do to a higher effective quench rate obtained in the high-energy sputtering techniques. Chien *et al.*<sup>5</sup> reported on the magnetic and structural properties of a wide range of Cu<sub>1-x</sub>Fe<sub>x</sub> alloys processed via dc magnetron sputter deposition. They were able to extend the fcc miscibility region up to 72 at. % Fe and the bcc miscibility region up to 38 at. % Cu.

In the past few years, much research has been performed on Fe-Cu alloys prepared via HEBM since it was shown that the miscibility of Fe in fcc Cu can be extended to  $\approx 60$  at. %.<sup>15,25,26,32,33</sup> This technique offers an alternative to rapid-quenching techniques to form metastable alloys of elements which are immiscible under equilibrium conditions. Uenishi *et al.*<sup>18</sup> report that the lattice parameter of bcc and fcc HEBM Cu-Fe alloys increase near linearly with increasing concentration of the dilute element, i.e., Cu in bcc Fe and Fe in fcc Cu, reaching a maximum for Cu<sub>50</sub>Fe<sub>50</sub>. By comparing the lattice parameters measured in HEBM powders to those measured in liquid-quenched ribbons and vapor-quenched thin films, Uenishi *et al.*<sup>18</sup> show the volume expansion is significantly larger in HEBM samples. From this it is clear that the HEBM samples have a local structure which must differ from those alloys produced by quenching techniques. It is likely that the difference in lattice parameter between the HEBM samples and those produced via vapor quenching is the result of the total strain energy of the system which varies with the processing technique.

### B. Electronic and magnetic properties

The electronic structure of the Fe atom has the Ar core with a  $3d^6 4s^2$  valence. However, when Fe is combined with other Fe atoms to form a metal, some of the lower level electrons are promoted. In the case of Fe, the  $3d$  majority band becomes nearly filled, 4.8 of 5 states, and the minority band has 2.6 of 5 states filled. The two  $4s$  states each have 0.3 occupancy. This configuration provides the  $2.2 \mu_B$  measured in bcc Fe. In addition, it is the strong  $3d$ - $3d$  interactions and their directionality constraints which dictate the bcc structure. Alternatively, the Cu atom has the Ar core with a  $3d^{10} 4s^1$  valence. In its metallic state both  $3d$  bands are filled and the two  $4s$  states are each half occupied.<sup>27</sup> With both  $3d$  bands filled, the Cu atom carries no magnetic moment. The strong interaction between Cu atoms in metallic Cu derive from the  $4s$  (and some degree of  $4p$ ) hybridization.<sup>34</sup>

When Cu is alloyed with Ni (Ar core +  $3d^8 4s^2$ ), the measured  $\mu_B$  per Ni atom shows a linear decrease with increasing Cu content. It was once believed that the addition of each Cu atom was equivalent to adding one electron to the alloy

which would then occupy the lowest energy state of the alloy which is in the 3d minority band of Ni.<sup>27</sup> When  $\approx 60\%$  of the atoms are Cu the net magnetization of the alloy becomes zero at 0 K.<sup>35</sup> However, more recent experimental<sup>36,37</sup> and theoretical<sup>38</sup> studies show the local 3d holes do not completely fill with the addition of Cu. Hence, the diminution of the magnetic moment may result from the depopulation of the majority band concurrent with the population of the minority band. In contrast, when Cu is alloyed with Fe, the magnetic moment per Fe atom does not change appreciably even at high Cu concentrations.<sup>4,5,26</sup> The magnetic moment behavior is characteristic of magnetic dilution, where the sample's saturation magnetization decreases linearly with increasing Cu but the  $\mu_B/\text{Fe}$  atom remains constant until the percolation limit is reached. The reason for this is that the high-density Fe d states are poorly matched in energy with the low-density Cu s states and little hybridization takes place.<sup>39</sup> As a result, the addition of Cu does not strongly influence the electronic structure of Fe near the Fermi surface and does not significantly disturb the magnetism of Fe. Additional evidence is the observation that the introduction of Cu does not force the Fe to strong ferromagnetism, which is defined by the filled majority spin band, until very high concentrations of Cu are present.<sup>5</sup>

Several authors have reported on the magnetic properties of HEBM Cu-Fe samples. Uenishi *et al.*,<sup>26</sup> in agreement with the thin film work of Chien *et al.*,<sup>5</sup> have shown that the moment per Fe atom is near  $2.2\mu_B$  for samples having Fe content greater than 50 at. %, but falls to zero for less than 20 at. % (i.e., at the onset of the percolation limit). Yavari, Desre, and Benameur<sup>15</sup> show a nearly equal magnetic moment at room temperature for the HEBM fcc  $\text{Cu}_{50}\text{Fe}_{50}$  phase and the equivalent decomposed state (i.e., a mixture of bcc Fe and fcc Cu).

These results qualitatively differ with the theoretical work of Fu and Freeman who investigated the electronic and magnetic properties of fcc Fe thin films in intimate contact with fcc Cu.<sup>40</sup> Although there are, of course, great differences between Fe-Cu alloys and thin Fe/Cu layers which limit the extent of comparison, some insight can be gained by studying the electronic interactions at the Fe-Cu interface. Specifically, Fu and Freeman, using the full-potential, linearized-augmented-plane-wave<sup>41</sup> approach to calculating electronic structure, found that the Fe-Cu interlayer distance was contracted by 3% relative to the Cu-Cu distance, i.e., from 1.805 to 1.75 Å. They also report an enhanced calculated magnetic moment on the Fe atom of  $2.85\mu_B$  when Fe is in intimate contact with Cu. These results may be a consequence of having an fcc Fe lattice parameter near that of Cu, whereas the Fe-Cu alloys studied here and others made by vapor quenching have lattice parameters significantly larger.

### III. EXPERIMENTAL

#### A. Materials processing

The samples in this study were processed using a Spex<sup>TM</sup> (Ref. 42) mill with elemental starting materials having 99.99% purity or better. The  $\text{Cu}_{70}\text{Fe}_{30}$  samples were processed at the Naval Research Laboratory (Washington, D.C.) by milling elemental powders of Fe and Cu for a period of 20 h with two 8 g steel balls having radii of  $\approx 6$  mm and two smaller 1 g balls having radii of  $\approx 3$  mm. The  $\text{Cu}_{50}\text{Fe}_{50}$

samples were produced at the Instituto de Magnetismo Aplicado (Madrid, Spain) using a Fritsch<sup>TM</sup> (Ref. 42) vibrating mill and starting materials of high-purity Fe powder and Cu foil. Milling was performed using a single 6 cm steel ball for a period of 400 h.<sup>20,25</sup> For both milling operations the elemental starting materials were carefully weighed and introduced into the mill which was then capped under an argon-gas environment to limit the amount of oxidation during milling.

#### B. Extended x-ray-absorption fine structure

The x-ray-absorption coefficients encompassing the Fe and Cu K absorption edges were collected using the X23B and X23A2 beamlines at the National Synchrotron Light Source (Brookhaven National Laboratories, Upton, New York). Both beamlines, X23B and X23A2, were designed for but not limited to EXAFS measurements. They both employ double-crystal, fixed-exit monochromators with beamline X23B using a pair of Si (111) crystals and X23A2 using a pair of Si (311) crystals. The EXAFS data were collected when the storage ring energy was 2.5 GeV with a current between 110 and 250 mA.

Because of strain hardening caused by the milling procedure, it was difficult to grind the powders to a suitable particle size for use with the EXAFS transmission data collection technique. Hence, we opted to use the total-electron-yield (TEY) data collection technique where we applied a generous amount of the powder over a still-wet coating of colloidal graphite on a substrate of commercial grade Al foil to construct the TEY sample. In TEY data collection the sample is used as the cathode in a He gas-flow ionization cell where the x-ray absorption is monitored by measuring the sample current induced by the by products of the core hole decay, namely the Auger and secondary electrons.

EXAFS data were collected from the milled powders and thin foils of Fe and Cu. The later data were collected in the transmission mode and used as empirical standards of the bcc and fcc structure, respectively. Prior to data collection, the detector circuit linearity was measured by comparing the ratio of the transmitted signal ( $I_t$ ), or in the case of TEY the sample current ( $I_s$ ), to the incident signal ( $I_0$ ), above the Fe and Cu absorption edges before and after the beam was attenuated 50%. The incident beam was attenuated by placing several layers of 0.01 in. commercial grade Al foil upstream of the sample and detectors. The linearity of the detector circuit was found to vary less than 0.5% indicating suitable conditions for data collection.

Following established EXAFS analysis procedures,<sup>43</sup> a line was fit to the preabsorption edge region and the area under this line and its extrapolation were removed from the spectrum. The extended fine structure appearing from 20–800 eV above the absorption edge were isolated and normalized to the edge step height and energy, thus putting all data on a per atom basis. Residual, nonoscillatory curvature in the data was eliminated by fitting and removing a cubic spline curve using three equidistant internal knots. These data were then converted to photoelectron wave-vector ( $k$ ) space and Fourier transformed to radial coordinates ( $r$ ).

The Fourier transform of the EXAFS data is similar in many respects to a partial radial distribution function (PRDF) obtained by the refinement of x-ray-scattering data.

The amplitudes of the peaks are typically proportional to the occupation and atomic disorder of the neighboring atom shells, and the radial distances of the peaks correspond to the bond distances between the central absorbing atom and its local neighbors.<sup>43</sup> The data in this form differ from a PRDF in that corrections for electron phase shifts have not yet been added, hence the radial distances of the Fourier peaks are offset from their true bond distances to lower  $r$  values. Notwithstanding, comparison between Fourier-transformed data and similarly analyzed data from empirical standards are useful in determining relative changes in the local structure and atom symmetry.

### C. EXAFS near-neighbor modeling using FEFF

Theoretical EXAFS data, generated using the FEFF (version 3.11) codes of Rehr *et al.*,<sup>44</sup> were analyzed in a manner similar to that discussed above. (Henceforth, these data will be referred to as FEFF data.) These data were used to fit Fourier-filtered (FF) Fe and Cu EXAFS data from the nearest-neighbor Fourier peak region ( $1 \text{ \AA} \leq r \leq 3 \text{ \AA}$ ) of the milled samples. The fitting was performed in  $k$  space where the phase and amplitude of the oscillations are fit with parametrized FEFF data to determine the local atomic parameters around the absorbing atoms, i.e., bond distances ( $r$ ), coordination numbers (CN), and the EXAFS Debye-Waller coefficients ( $\sigma^2$ ). The latter is a measure of both the static and thermal displacement of atoms about a mean bond distance.

Quantitative information of the local structure and chemistry around the Fe and Cu sites was obtained by fitting the nearest-neighbor peak region of the Fourier-transformed Fe and Cu EXAFS data with FEFF data. In performing this fitting analysis, a data range in  $r$  space that encompassed the nearest-neighbor peak ( $1 \text{ \AA} \leq r \leq 3 \text{ \AA}$ ) was selected and back-Fourier transformed (i.e., Fourier-filtered) to  $k$  space. In  $k$  space, the phase and amplitude of the nearest-neighbor FF EXAFS data were fit using the parametrized FEFF data. The quality of the fit was judged by a least-squares fitting parameter ( $\chi^2$ ). During the fitting analysis of both the Cu and Fe standards, and the data collected from the milled samples, the  $r$  of contributing atom shells were floated while all other parameters were fixed at their theoretical values. Once approximate values of the radial distances were determined, additional fits were carried out in which the  $r$  values were fixed and the CN and  $\sigma^2$  values were allowed to vary. Further refinement of the fit was achieved by fixing the CN and  $\sigma^2$  values at the fitted values and again varying  $r$  using the previously determined values as the starting values. Finally, all parameters were floated from the starting values determined from the above approach until a best fit for all parameters was obtained. At no time was the number of fitting parameters greater than the maximum number allowed by the Nyquist theorem, i.e.,  $(2\Delta k \Delta r)/\pi$ .<sup>45</sup> The best fits for the Cu and Fe standards were further refined by systematically varying the edge energy correction,  $v_0$ , and the amplitude reduction coefficient,  $S_0^2$ , until the  $\chi^2$  fitting parameter was optimized.

## IV. RESULTS AND DISCUSSIONS

### A. X-ray-diffraction measurements

X-ray-diffraction measurements of the milled powders were performed using a Philips<sup>TM</sup> (Ref. 42) diffractometer

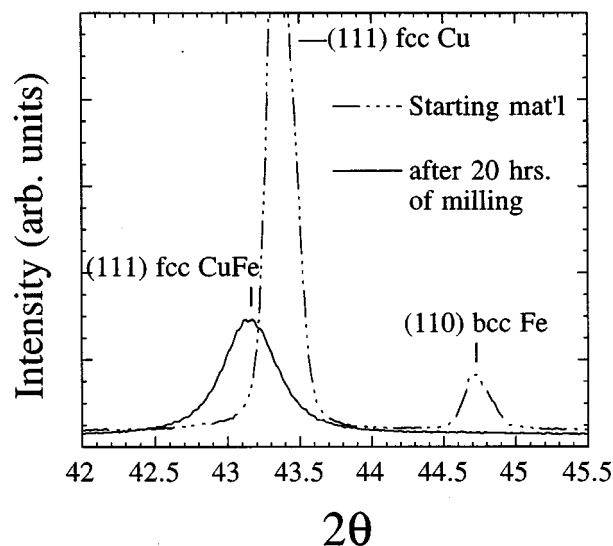


FIG. 1. A portion of the  $\theta$ - $2\theta$  x-ray-diffraction scan of the  $\text{Cu}_{70}\text{Fe}_{30}$  material before and after HEBM illustrating the disappearance of the (110) bcc Fe peak and the shift of the (111) fcc Cu peak to a higher  $d$  spacing.

equipped with a fixed anode, Cu  $K\alpha$  source. Figure 1 is a plot of a portion of the  $\theta$ - $2\theta$  scan for the  $\text{Cu}_{70}\text{Fe}_{30}$  sample before and after milling. The asymmetry of the Fe(110) peak in the scan of the starting materials is caused by the unfiltered  $K\alpha_2$  radiation having  $\lambda = 1.544 \text{ \AA}$ . These data are representative of both milled samples with slight differences corresponding to the change in the lattice parameter between the two samples. In Fig. 1 it is clear that after 20 h of milling, the bcc(110) peak of Fe has completely disappeared and that the fcc(111) peak of Cu has significantly shifted to a higher  $d$  spacing. This signals that the Fe atoms now exist in the fcc phase. The absence of a second family of fcc peaks suggests that the Fe and Cu atoms coexist in a single fcc phase. Lattice parameters of  $3.641 \pm 0.005 \text{ \AA}$  and  $3.634 \pm 0.003 \text{ \AA}$  were calculated for the  $\text{Cu}_{50}\text{Fe}_{50}$  and  $\text{Cu}_{70}\text{Fe}_{30}$  samples, respectively. These values are significantly greater than the values predicted by Vegard's law,  $3.6025 \text{ \AA}$  for  $\text{Cu}_{50}\text{Fe}_{50}$  and  $3.6075 \text{ \AA}$  for  $\text{Cu}_{70}\text{Fe}_{30}$ , representing an expansion of 3.24% and 2.22% in volume, respectively. The expansion in the lattice constant of the HEBM Cu-Fe samples has been shown to increase with both increased milling time and increased Fe concentration peaking near 50 at. %, suggesting that the expansion is due to the progressive incorporation of Fe into the Cu lattice.<sup>15</sup> The lattice parameters measured here are comparable to those measured by Uenishi *et al.* for HEBM Cu-Fe samples.<sup>26</sup> Similar to the values of Uenishi *et al.*, these are larger than those measured for vapor-quenched<sup>4,5</sup> and liquid-quenched samples.<sup>46</sup> It is likely that the difference between the values for HEBM samples and those processed using liquid- and vapor-quenching techniques is due to the total strain energy in the lattice introduced by the processing technique.

The lattice expansion induced by the introduction of the Fe atoms to the Cu matrix via HEBM suggests that within this environment the atomic radii of the Fe and/or Cu atoms are different compared with those of their pure phase states. It is well known that the average atomic radius of an element can change considerably depending upon the environment in

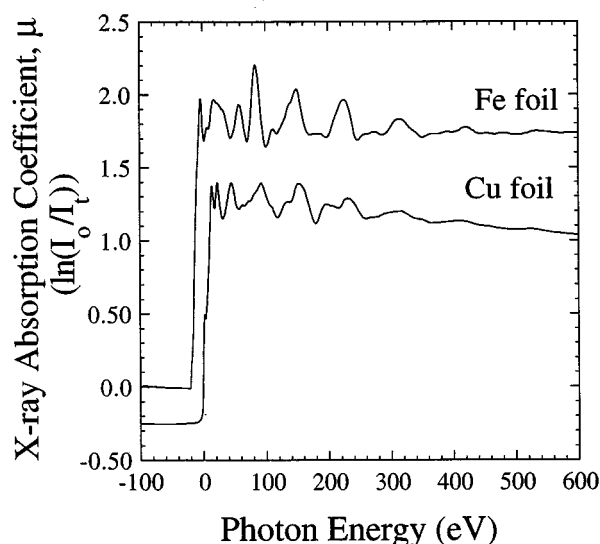


FIG. 2. X-ray-absorption coefficient [as the  $\ln(I_0/I_t)$  where  $I_t$ =transmitted signal,  $I_0$ =incident signal] encompassing the Fe and Cu  $K$  absorption edges in Fe and Cu foils, respectively. The Cu data have been shifted in energy and vertically offset to avoid overlapping the Fe data.

which it is placed. Typically, these changes are determined by measurements made via x-ray diffraction (XRD) where small changes in the unit cell dimensions can be measured with great accuracy. Using this approach, one obtains a measure of the average local distortion to the lattice caused by the introduction of one element into another, but it is unclear which element changes size. By applying EXAFS, an element-specific local probe, one should be able to discern if the lattice expansion is the result of an isotropic dilation of all bonds or if it is due to a specific atom pair correlation.

These XRD results suggest that the HEBM Cu-Fe samples exist as a single fcc phase. They do not provide information concerning the local chemical homogeneity of the samples and therefore it remains possible that small fcc Fe clusters have stabilized coherently within the fcc Cu lattice.<sup>47</sup> To address this issue we have pursued x-ray-absorption fine-structure studies of these samples which will provide information of the local structure and chemistry around the Cu and Fe sites. The results of that study are presented in Sec. IV C.

#### B. Extended x-ray-absorption fine-structure analysis of fcc Cu and bcc Fe standards

Figure 2 is a plot of the x-ray-absorption coefficients [ $\mu=\ln(I_0/I_t)$ ] encompassing the Fe and Cu  $K$  absorption edges collected from the Fe and Cu foil standards, respectively. The oscillations appearing above the edges are the fine structure of EXAFS and arise from the modulation of the x-ray-absorption coefficient from the interference of the outgoing and backscattered photoelectron waves caused by absorption. These oscillations contain information on the local environment around the absorbing atoms. The data from the Fe and Cu foils are used here as empirical standards of the bcc and fcc structures as well as chemical standards for the modeling of the Fe and Cu EXAFS data collected from the milled samples. One sees in comparing the Fe and Cu data of Fig. 2 that there are pronounced differences in the

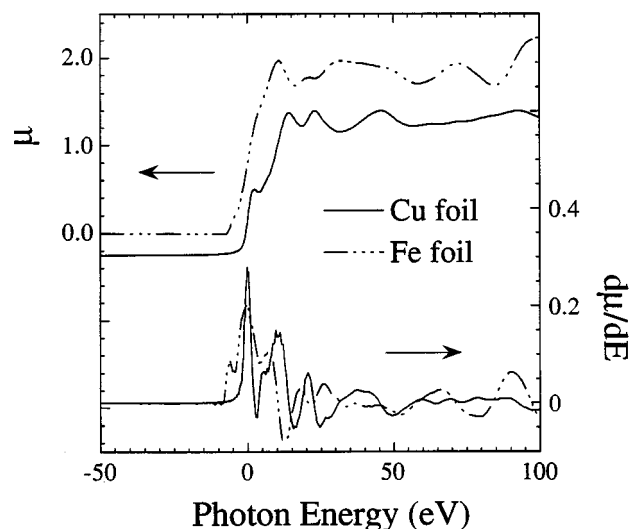


FIG. 3. X-ray-absorption near-edge fine structure (XANES) for the Fe and Cu  $K$  absorption edges collected from Fe and Cu foils, respectively. The Fe data have been vertically offset to allow direct comparisons to the Cu data. The curves positioned on the lower portion of the figure are derivatives of these same data.

fine structure between these data sets. These differences are most noticeable in the near-edge fine structure including the edge region and extending to  $\approx 150$  eV above the edge.

Figure 3 illustrates an expanded view ( $-50$ – $100$  eV) of the near-edge region and the derivative of the same. The derivative is supplied to more clearly contrast the differences between data sets in the near-edge region. The structure appearing very near the absorption edge is referred to as the x-ray-absorption near-edge structure, or XANES, and contains information more heavily weighted by the local atom symmetry and the density of states. In this figure, one sees that the Cu data have a small peak appearing halfway up the absorption edge step which is absent in the Fe data. In addition,

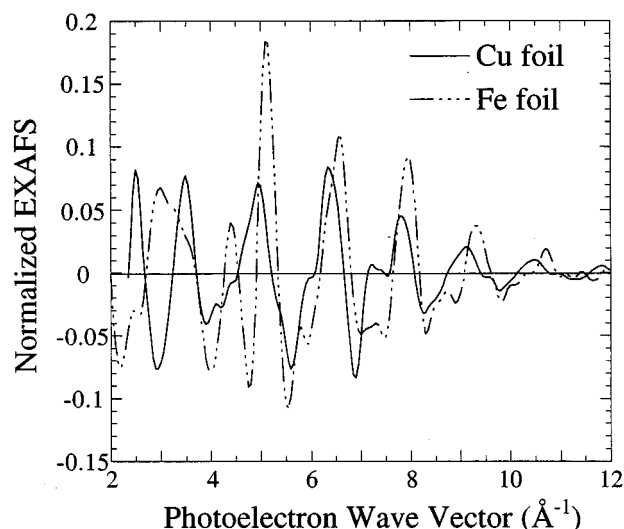


FIG. 4. Normalized EXAFS data after background removal and conversion to photoelectron wave-vector space collected from the Fe foil (dashed curve) and the Cu foil (solid curve). Data sets are plotted using the same  $x$  and  $y$  axes to allow direct comparisons.

tion, the Cu data show a pronounced splitting near 20 eV which again is absent from the Fe profile. At higher energies, the oscillations are considerably out of phase with each other indicating differences in atomic symmetry.

After background removal and normalization of the extended fine structure to the edge energy and step height, the data are converted to  $k$  space (see Fig. 4). In this form, the EXAFS can be directly compared and contrasted more clearly in terms of their phase and amplitude. The largest differences seen in Fig. 4 are the splitting of the Cu EXAFS near  $3 \text{ \AA}^{-1}$ , which is absent in the Fe, and the splitting of the Fe EXAFS near  $5 \text{ \AA}^{-1}$ , which is absent in the Cu. The great differences between Cu and Fe EXAFS data arise primarily because of the differences in the local atom symmetry in their respective structures. Cu has a face-centered-cubic (fcc) structure which is a close-packed cubic arrangement of atoms. Because of an incomplete  $d$  shell, Fe does not assume a close-packed structure but instead takes a body-centered-cubic (bcc) structure where the atom arrangement satisfies the directionality of the  $d$ -shell wave functions. Taking a corner atom as our 0th atom (0,0,0), the bcc structure has as

its nearest-neighbors to the 0th atom the eight body-centered atoms ( $1/2, 1/2, 1/2$ ) at a distance of  $2.482 \text{ \AA}$ . Its next-nearest neighbors are the six cube edge sites at a distance of  $2.866 \text{ \AA}$  (i.e., the lattice parameter). In contrast, the fcc structure has as its nearest neighbors the 12 face-centered atoms ( $1/2, 1/2, 2/0$ ) at  $2.556 \text{ \AA}$  and next the six cube edge sites at  $3.615 \text{ \AA}$ .

Figure 5 is a plot of the Fourier-transformed EXAFS data for the Cu (solid curve) and Fe (dashed curve) standards. Presented above this plot are depictions of the bcc and fcc unit cells. In each of these panels are  $\mathbf{r}$  vectors which originate at the central atom and extend to the near neighbors. These vectors correlate with features in the Fourier profiles presented in the main panel to indicate which atom correlations contribute to the Fourier peaks. Because the Fe EXAFS has a limited  $r$ -space resolution of  $\approx 0.4 \text{ \AA}$ , the first two neighbors of the bcc unit cell contribute to the first Fourier peak in the Fe profile centered near  $2.1 \text{ \AA}$ . For this reason, this peak appears much broader than the corresponding peak in the Cu EXAFS which has 12 nearest neighbors located at a single distance of  $2.556 \text{ \AA}$ . Recalling that the Fourier transform of EXAFS data is uncorrected for electron phase shifts, the peaks do not correspond directly to the true bond distances but are instead shifted to lower  $r$  values. For example, the Cu nearest-neighbor peak is seen in Fig. 5 to be centered at  $2.125 \text{ \AA}$  whereas the actual distance is  $2.556 \text{ \AA}$ , indicating a phase shift for this correlation of  $\approx 0.43 \text{ \AA}$ . The large peak centered near  $4.5 \text{ \AA}$  in the Fourier transform of the bcc Fe EXAFS contains amplitude contributions not only from the 24  $\mathbf{r}_4$  and eight  $\mathbf{r}_5$  neighbors but also from a photoelectron focusing effect caused by the collinear arrangement of the center-body-centered ( $\mathbf{r}_1$ )-body-diagonal ( $\mathbf{r}_5$ ) sites. This feature is a useful fingerprint for bcc structures. A similar amplitude enhancement is observed in the fcc Cu profile near  $4.8 \text{ \AA}$  where the center-face-centered ( $\mathbf{r}_1$ )-face diagonal ( $\mathbf{r}_4$ ) sites are arranged collinear with respect to one another.

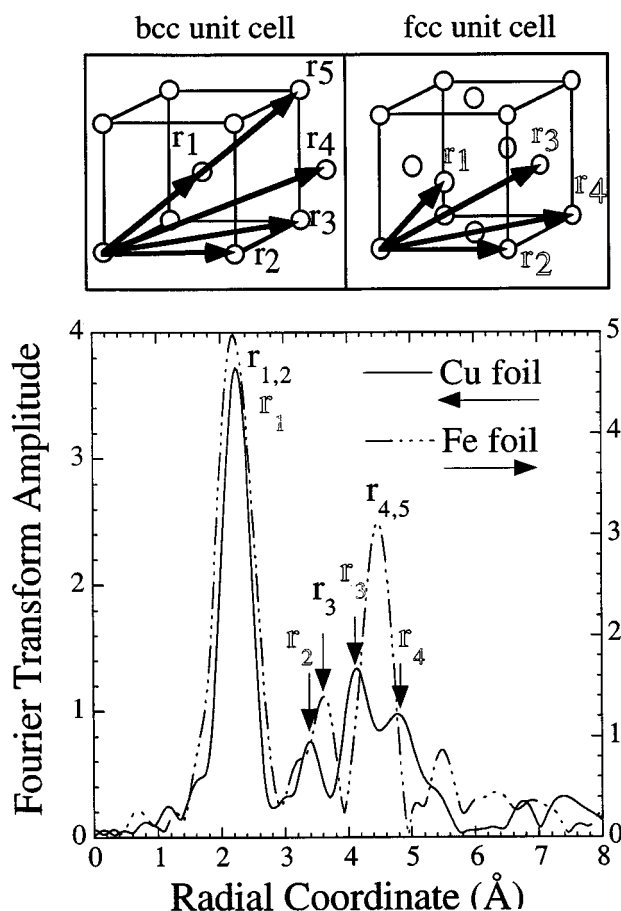


FIG. 5. Fourier-transformed Cu and Fe EXAFS data collected from Cu and Fe foils, respectively. Panels located above the plot depict the bcc and fcc unit cells with vectors from the central atom to the near neighbors. Vectors listed on the plot indicate which atomic pair correlations contribute to the Fourier peaks. All data were transformed using  $k^2$  weighting and  $k$  ranges of  $2.5$ – $12.5 \text{ \AA}^{-1}$ . Electron phase shift corrections have not been included in these data, therefore, radial distances do not correspond directly to bond lengths (see text).

### C. Extended x-ray-absorption fine-structure analysis of HEBM Cu-Fe samples

Figure 6 is a plot of the x-ray-absorption as the normal-

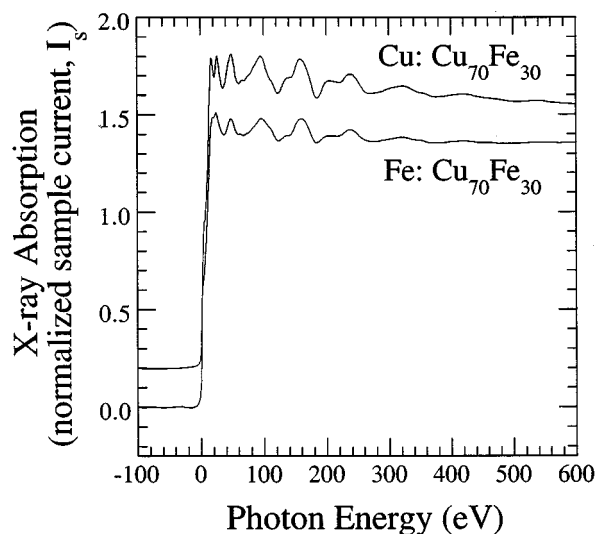


FIG. 6. X-ray-absorption, as normalized sample current ( $I_s/I_0$ ) versus photon energy, for the Fe and Cu  $K$  absorption edges in the HEBM  $\text{Cu}_{70}\text{Fe}_{30}$  sample. The Cu data have been vertically offset so as not to overlap the Fe data.

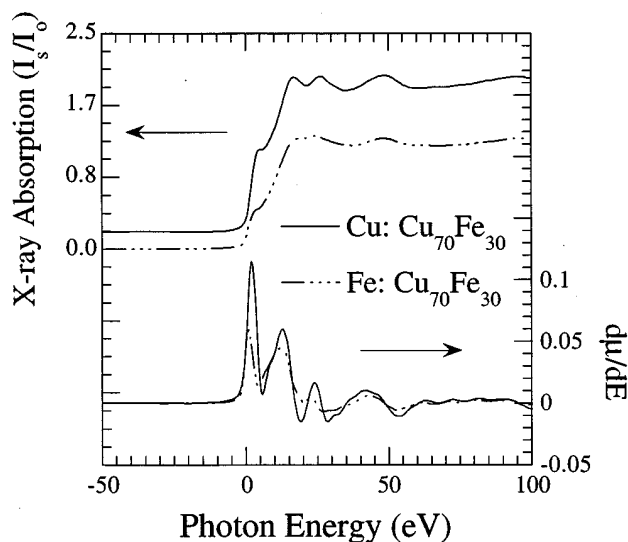


FIG. 7. X-ray-absorption near-edge fine structure (XANES), as normalized sample current  $[I_s(E)/I_0(E)]$  versus photon energy, for the Fe and Cu  $K$  absorption edges collected from the HEBM  $\text{Cu}_{70}\text{Fe}_{30}$  sample. The Cu data have been vertically offset so as not to overlap the Fe data. The curves positioned on the lower portion of the figure are derivatives of these same data.

ized sample current ( $I_s/I_0$ ), encompassing the Fe and Cu  $K$  absorption edges collected from the milled  $\text{Cu}_{70}\text{Fe}_{30}$  sample. The Cu data are vertically offset from the Fe data to allow comparison between data sets. These data are qualitatively similar to the  $\text{Cu}_{50}\text{Fe}_{50}$  sample. As is readily seen in Fig. 6, the Cu and Fe data appear similar. The extended fine structure of both data sets displays oscillations having similar phase and relative amplitudes while the near-edge regions are also similar (see Fig. 7) with some exceptions. In particular, some of the features appearing in the Cu spectrum appear to be less resolved in the Fe data. Because the energy resolution at the Fe edge (7111 eV) is slightly better than that of the Cu edge (8979 eV), this effect cannot be attributable to beamline optics, but instead is likely characteristic of the electronic structure of Fe in the fcc symmetry. The derivative of the XANES illustrates similarities in the Fe and Cu near-edge data, with every feature in the Cu data represented in the Fe data. From these data one can conclude that both Fe and Cu share a similar structure having the same atomic symmetry.

Figure 8 contains the Fe and Cu EXAFS from the  $\text{Cu}_{70}\text{Fe}_{30}$  sample after normalization and conversion to  $k$  space (see Sec. III B). Data collected from a Cu foil are similarly analyzed and presented as a standard of the fcc structure. In this form, the data can be compared in terms of phase and amplitude of the EXAFS oscillations to determine similarities or differences between samples and also to provide information as to the signal-to-noise characteristics of the experiment. Error bars are presented on both the Cu and Fe data in Fig. 8 but are difficult to see because of their small size. These error bars represent one standard deviation from the mean calculated by merging five data sets after normalization and conversion to  $k$  space. As such, they reflect both the data collection statistics and any uncertainty introduced to the data from the background removal procedures. The very small amplitudes of the error bars illustrate the excellent

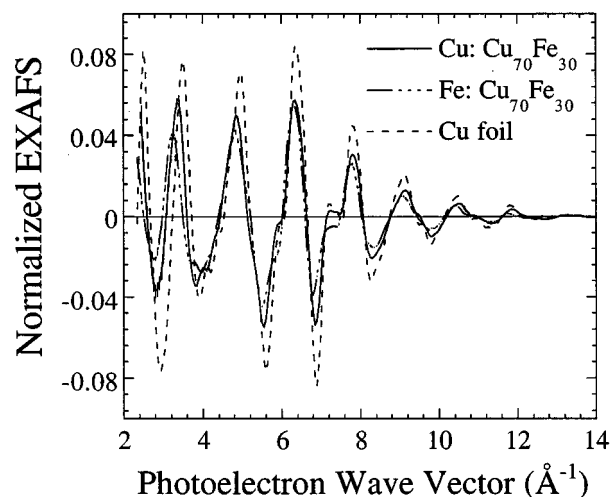


FIG. 8. Normalized EXAFS data after background removal and conversion to photoelectron wave-vector space for Fe (dash-dot-dot curve) and Cu (solid curve) in the HEBM  $\text{Cu}_{70}\text{Fe}_{30}$  sample. Similar data collected from the Cu foil (dashed curve) is also presented as a standard of the fcc structure. Data sets are plotted using the same  $x$  and  $y$  axes to allow direct comparisons.

signal-to-noise of the data collection from these samples. Qualitative comparisons between these data, and with the data of the fcc Cu standard, indicate that both the Fe and Cu atoms in the milled samples exist in a close-packed structure similar to that of fcc Cu. Subtle differences between the data sets for the milled sample versus that of the Cu foil, namely, the reduced amplitude of the oscillations and the slight offset in phase at low  $k$  values, can be attributed to the increased structural disorder in the milled samples arising from the impact nature of the HEBM technique and differences in the local chemistry between the standard and milled samples. At this early stage in the analysis, the meaning of these subtle differences is difficult to relate to specific changes in local structure or chemistry. For this reason these data are Fourier transformed to radial coordinates in order to obtain direct information of the structure and atomic symmetry around the absorbing atoms.

The Fourier-transformed EXAFS data from the  $\text{Cu}_{50}\text{Fe}_{50}$  sample are presented in Fig. 9. These data are similar to the data collected from the  $\text{Cu}_{70}\text{Fe}_{30}$  sample. The Fe and Cu EXAFS from the milled sample are presented on the same  $x$  and  $y$  axes without normalization or offset to allow direct comparisons to be made. The data corresponding to the Cu standard are presented on the same  $x$  axis but different  $y$  axis in order to allow an improved comparison between the data from the milled samples and the standard at the higher radial distances (i.e.,  $r \geq 3$  Å). A schematic of the fcc unit cell is presented in the inset panel which indicates which atom correlations contribute to the Fourier peaks. The differences in peak amplitude between the Cu and Fe EXAFS in the milled samples and the Cu standard are likely due to an increase in the static displacement component to the EXAFS Debye-Waller coefficient caused by the ballistic nature of the processing and not due to any significant change in the coordination around the absorbing atoms. Data corresponding to the milled samples are shown in Fig. 9 to resemble closely the fcc structure of the Cu standard in both the relative am-

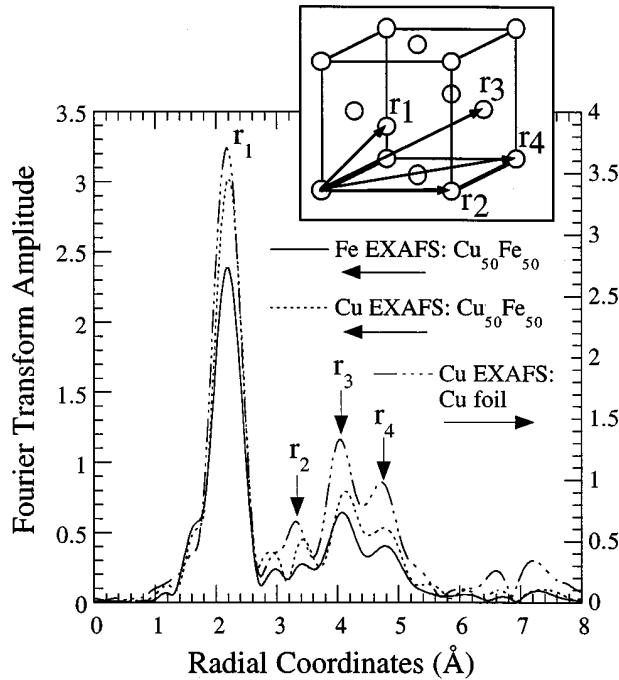


FIG. 9. Fourier-transformed Fe and Cu EXAFS data collected from the HEBM  $\text{Fe}_{50}\text{Cu}_{50}$  sample with similar data collected from a fcc Cu standard shown for comparison. All data were transformed using  $k^2$  weighting and  $k$  ranges of 2.5–12.5  $\text{\AA}^{-1}$ . Electron phase-shift corrections have not been included in these data, therefore radial distances do not correspond directly with bond lengths (see text).

plitude and radial distance of Fourier peaks appearing over the  $r$  range of 1.5 to 5.5  $\text{\AA}$ . Among the differences between these data are a slight shift of the nearest-neighbor ( $r_1$ ) and next-nearest-neighbor ( $r_2$ ) peaks; this latter peak corresponds to the lattice parameter. These shifts suggest that the nearest-neighbor bond is greater in the milled sample than in the fcc Cu standard, a result that is consistent with the larger lattice parameter measured in the milled samples using x-ray diffraction. The Fourier-transformed EXAFS data of Fig. 9 establish that both Fe and Cu unambiguously reside in fcc structures. It precludes the existence of any significant amount of bcc Fe clusters, which are the more energetically favorable structure for Fe at room temperature. However, these data do not rule out the possibility that some Fe exists in small fcc clusters, chemically segregated, but structurally coherent, within the fcc Cu matrix. In order to determine if indeed this is the case, a quantitative study of the near-neighbor environment was undertaken.

#### D. Near-neighbor modeling of the extended x-ray-absorption fine structure Near-neighbor chemistry

Quantitative information on the local structure and chemistry around the Fe and Cu sites in both the standards and the HEBM samples was obtained by fitting the nearest-neighbor peak region of the Fourier-transformed Fe and Cu EXAFS data with FEFF data. The finer details of the fitting methodology are presented in Sec. III C. The results of the fitting analysis of the standards and HEBM samples are presented

TABLE I. Structural parameters used to obtain best fits to Fourier-filtered EXAFS data. Note: The error bars listed are derived from comparing the best fits between the mean and mean  $\pm 1$  std. dev. They represent a 25% increase in the  $\chi^2$  fitting parameter.

Pair correlations	Bond distance ( $\text{\AA}$ )	Coordination number	$\sigma_{300\text{ K}}^2$ ( $\text{\AA}^2$ )
<i>bcc Fe</i> ( $S_0^2=0.85$ ; $\nu_0=-2.5$ eV)			
Fe-Fe	$2.49 \pm 0.005$	$7.5 \pm 0.2$	$0.0047 \pm 0.0002$
Fe-Fe	$2.84 \pm 0.01$	$6.5 \pm 0.2$	$0.0112 \pm 0.0005$
Theoretical			
Fe-Fe	2.482	8	
Fe-Fe	2.866	6	
<i>fcc Cu</i> ( $S_0^2=0.88$ ; $\nu_0=0$ )			
Cu-Cu	$2.54 \pm 0.005$	$12 \pm 0.2$	$0.0085 \pm 0.0003$
Theoretical			
Cu-Cu	2.556	12	
<i>Cu<sub>50</sub>Fe<sub>50</sub></i>			
Fe-Fe	$2.52 \pm 0.005$	$5.2 \pm 0.3$	$0.0083 \pm 0.0008$
Fe-Cu	$2.63 \pm 0.01$	$6.3 \pm 0.3$	$0.0146 \pm 0.0004$
Cu-Fe	$2.63 \pm 0.01$	$4.9 \pm 0.3$	$0.0121 \pm 0.0005$
Cu-Cu	$2.54 \pm 0.005$	$5.9 \pm 0.3$	$0.0085 \pm 0.0005$
<i>Cu<sub>70</sub>Fe<sub>30</sub></i>			
Fe-Fe	$2.52 \pm 0.005$	$2.5 \pm 0.2$	$0.0066 \pm 0.0008$
Fe-Cu	$2.62 \pm 0.01$	$8.3 \pm 0.4$	$0.0110 \pm 0.0004$
Cu-Fe	$2.62 \pm 0.01$	$8.0 \pm 0.4$	$0.0099 \pm 0.0005$
Cu-Cu	$2.54 \pm 0.005$	$2.7 \pm 0.2$	$0.0089 \pm 0.0005$

in Table I. Also listed in this table are the  $S_0^2$  and  $\nu_0$  values which were used to provide the best fit between theory and experiment for the Cu and Fe standards. It is noteworthy that the difference between the fitting parameters for the standards and their theoretical values are  $\approx 6$ –7 % in CN and  $\approx 1\%$  in  $r$ . Some of these differences can be attributed to the uncertainty related to data collection statistics and the background removal procedures. This uncertainty translates to a 25% increase in the  $\chi^2$  fitting parameter. This was determined by fitting the mean  $\pm$  one standard deviation with no adjustable parameters using the best-fit parameters which were determined by fitting only the mean. If one systematically steps the values for the best-fit parameters and monitors the change in  $\chi^2$ , one finds that the error bars in Table I double for a 100% increase in  $\chi^2$ . The errors between the FEFF-calculated and theoretical nearest-neighbor  $r$  for fcc Cu is consistent with the results of Mansour, Wong, and Brizzolara<sup>48</sup> who found that the FEFF-generated bond distances are often smaller than the theoretical values.

During the fitting of the data from the HEBM samples, the  $\nu_0$  and the  $S_0^2$  values determined by the fitting of the standards, were applied directly and a similar approach of fitting refinement was followed. Although the backscattering amplitudes of Cu and Fe are very similar, sufficient differences exist in the phases to differentiate the Cu and Fe neighbors and allow the determination of the average local composition around the absorbing atoms. The error bars listed on the fitting parameters were determined by fitting the mean of the experimental data plus one standard deviation. The standard deviation of the data was calculated by merging five data scans after the background removal and conversion to  $k$ -space procedures. When the best-fit parameters for the mean data set were used to fit the mean  $\pm$  one standard deviation data, the  $\chi^2$  parameter increased by 25%. One sees



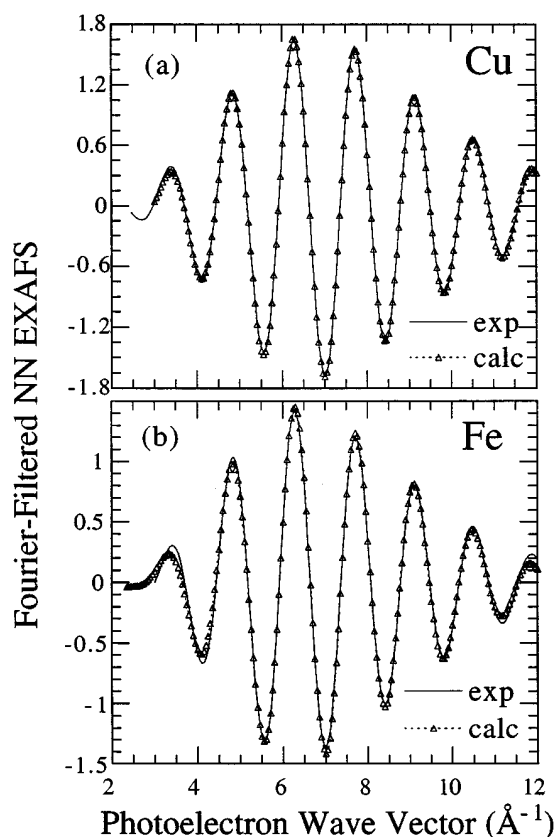


FIG. 10. Fourier-filtered, near-neighbor Cu (a) and Fe (b) EXAFS data (solid curves) for the HEBM  $\text{Cu}_{70}\text{Fe}_{30}$  sample with the best fit data (dashed curve with symbols) obtained via least-squares fitting of parametrized EXAFS spectra generated using FEFF ver. 3.11 codes (Ref. 44). An  $r$ -space range of 1–3  $\text{\AA}$  was Fourier-filtered from the EXAFS data presented in Fig. 9. The parameters used in these fits are listed in Table I.

that the error bars determined this way are quite small, representing a 0.2–0.3 % deviation from the mean value for  $r$ , a 5–6 % deviation from the mean value for CN, and a  $\approx 10\%$  deviation from the mean value for  $\sigma^2$ . From this, one can see that near-neighbor chemistry can be determined using this technique with modest certainty. This allows one to determine the approximate nearest-neighbor chemistry and unambiguously establish if significant amounts of atomic mixing have occurred.

The nearest-neighbor FF Cu and Fe EXAFS from the  $\text{Cu}_{70}\text{Fe}_{30}$  sample and the best fit for both are presented in Figs. 10(a) and 10(b). These data and fits are representative of the  $\text{Cu}_{50}\text{Fe}_{50}$  sample. The parameters corresponding to these fits are listed in Table I. For both samples, the best fit resulted from the use of two atomic shells, one of Fe and the other of Cu, simulating a mixed chemistry in the first coordination sphere. Prior to arriving at this model we had tried to fit the data using a single atomic shell of one or the other atomic species. This led to relatively poor fits as judged by visual inspection and the value of the  $\chi^2$  parameter. Attempts to provide a mixed chemistry in the nearest-neighbor environment by using two shells constrained to a single adjustable radial distance was found to greatly improve the fit. However, removing the single-distance constraint resulted in further improvements in the fit with the radial distances of

each shell converging to the values listed in Table I. Attempts to simulate fcc Fe clusters within a Cu fcc matrix by forcing the nearest-neighbor chemistry around Fe to be enriched with Fe neighbors resulted in a poor fit as judged by the  $\chi^2$  parameter. As is readily seen in Table I, the fitting of the Cu EXAFS resulted in parameter values which are consistent and complementary to those of the Fe EXAFS analysis. The ratio of Cu and Fe coordination numbers indicates that the first coordination sphere for the  $\text{Cu}_{50}\text{Fe}_{50}$  sample consists of a  $\text{Cu}_{54}\text{Fe}_{46}$  stoichiometry. This is supported by the independent modeling of both the Fe and Cu EXAFS. Energy-dispersive x-ray spectroscopy (EDXS) measurements on this sample indicate that the stoichiometry after milling is  $\text{Cu}_{48}\text{Fe}_{52}$ . Presumably, the slight increase in the Fe content is due to contamination from the steel balls and container introduced during the milling. The EXAFS calculated stoichiometry agrees with the EDXS results within the uncertainty of the measurement, and clearly indicates that the first coordination sphere consists of a mixed chemistry near to that measured via EDXS. Similarly, the first coordination sphere for the  $\text{Cu}_{70}\text{Fe}_{30}$  sample is measured to have a  $\text{Cu}_{75}\text{Fe}_{25}$  stoichiometry. Again, this value is consistent with the nominal values within the uncertainty of the analysis established by the fitting of the mean  $\pm$  one standard deviation.

#### Bond distances and atomic radii

The measured nearest-neighbor bond distances for like and unlike atom pairs, for both the  $\text{Cu}_{50}\text{Fe}_{50}$  and the  $\text{Cu}_{70}\text{Fe}_{30}$  samples, are presented in Table I. These data allow the calculation of lattice parameters solely from the results of the EXAFS fitting analysis. Taken together, the resulting EXAFS calculated lattice parameters are  $3.649 \pm 0.014$   $\text{\AA}$  and  $3.637 \pm 0.010$   $\text{\AA}$ , for the  $\text{Cu}_{50}\text{Fe}_{50}$  and the  $\text{Cu}_{70}\text{Fe}_{30}$  samples, respectively. These values match the values obtained by XRD measurements,  $3.641 \pm 0.005$   $\text{\AA}$  and  $3.634 \pm 0.003$   $\text{\AA}$ , within the uncertainty of the EXAFS and XRD analyses. This agreement indicates that the lattice expansion measured when Fe is introduced into the Cu lattice is due to the bond dilation experienced by the unlike atom pairs. It is noteworthy that dilated bonds have been reported in other binary transition-metal solid solutions. Using x-ray diffuse scattering, Ice *et al.* reported the dilation of Fe-Fe bonds in Fe-Ni solid solutions<sup>49</sup> and attribute this effect to an electron kinetic energy of the Fe atom when it resides on a large-volume, high-spin site. Reinhard *et al.*<sup>50</sup> performed similar studies of Fe-Cr and found a contraction of the Fe-Fe and Cr-Cr distances, while Schonfeld *et al.*<sup>51</sup> studied the Ni-Cr alloys and found a dilated Cr-Ni bond.

The EXAFS calculated nearest-neighbor bond distance for the atom correlations listed in Table I allow the deduction of the atomic radii for Fe and Cu in the alloys as well as the standards. These values are listed in Table II with similar values determined from XRD measurements and those calculated by Goldschmidt<sup>52</sup> and Pauling.<sup>53–55</sup> The values provided by Goldschmidt derive from an interpolation using Vegard's law and XRD measurements. He calculates atomic radii for different coordination using simple rules of contraction, for example, a 3% contraction when going from a coordination of 12 to 8, 4% for 12 to 6, and 12% when going from 12 to 4. Although these relationships were derived from empirical studies using salts, they provide a useful approxi-

TABLE II. Atomic radii calculated from near-neighbor EXAFS modeling compared with values calculated by Goldschmidt and Pauling assuming a coordination of 12 (except where indicated).

Sample	Atom correlation	EXAFS (Å)	XRD (Å)	Goldschmidt (Å)	Pauling (Å)
Fe foil	Fe-Fe	1.245 ±0.0025	1.241	1.24 <sup>a</sup>	
Cu foil	Cu-Cu	1.270 ±0.0025	1.278	1.28	1.276
Cu <sub>50</sub> Fe <sub>50</sub>	Fe-Fe	1.265 ±0.0025		1.27	1.26
Cu <sub>50</sub> Fe <sub>50</sub>	Cu-Cu	1.275 ±0.0025		1.28	1.276
Cu <sub>50</sub> Fe <sub>50</sub>	Fe-Cu	1.3125±0.005	1.2873±0.0018 <sup>b</sup>		
Cu <sub>70</sub> Fe <sub>30</sub>	Fe-Fe	1.260 ±0.0025		1.27	1.26
Cu <sub>70</sub> Fe <sub>30</sub>	Cu-Cu	1.270 ±0.0025		1.28	1.276
Cu <sub>70</sub> Fe <sub>30</sub>	Fe-Cu	1.310 ±0.005	1.2848±0.0011 <sup>b</sup>		

<sup>a</sup>Calculated assuming a coordination of 8.

<sup>b</sup>This represents the average atomic radii determined from XRD, no distinction is made concerning the individual atom pair correlations.

mation of atomic radii in metallic alloys. Pauling's values are based upon his postulation that the interatomic forces in metals can be modeled as resonating covalent bonds among the available atomic positions. He calculates the atomic radii using a relationship which accounts for both the number of available bonds, determined by valence, and the radius of a single resonant bond.<sup>54-56</sup>

In Table II one sees that the EXAFS-calculated atomic radii for the Cu and Fe standards are in good agreement with those measured by XRD and those calculated by both Goldschmidt and Pauling. Although there are statistically significant differences, that likely stem from the limitations of the EXAFS simulation codes, as a whole these differences are small and the agreement is excellent. In contrast, the average atomic radii calculated by EXAFS for the unlike atom pair correlations are very much larger than the values calculated

by Goldschmidt and Pauling, by 2.75 and 3.33 %, respectively.

Presented in Fig. 11 are the lattice parameters of Cu-Fe alloys calculated via the EXAFS fitting results, measured by XRD, calculated using the atomic radii of Goldschmidt and Pauling, and predicted by Vegard's law. As one would expect, the values calculated using the sum of the Goldschmidt radii plot very near to those predicted by Vegard's law. In contrast, values calculated using the sum of the Pauling radii fit closely to Vegard's law for low Fe concentrations but deviate for high Fe concentrations. The two XRD-measured lattice parameters determined for the HEBM samples studied here are shown to deviate positively from Vegard's law. These values are in very good agreement with other values measured for HEBM Cu-Fe samples,<sup>26</sup> but are larger than values measured for vapor-quenched Cu-Fe films.<sup>4</sup> The values calculated using the discrete bond distances determined by the EXAFS modeling plot on a parabola which deviates positively from Vegard's law. These later values, with error bars, are shown to encompass the XRD-measured lattice parameters for the two samples studied here and the values of Uenishi *et al.* for other HEBM Cu-Fe samples. This is strong evidence that the EXAFS fitting results represent the real physical state of the sample.

#### E. Origins of the Cu-Fe bond dilation

Figure 12 is schematic representation of an arrangement of Cu and Fe atoms which is consistent with the EXAFS modeling results presented in Tables I and II and Fig. 11. In this figure, the solid-line circles represent atom sites on an undistorted fcc lattice while the hashed circles represent Fe and Cu atoms slightly displaced from these sites. (The dashed-line circles represent sites which lie on planes beneath the surface layers.) The Cu and Fe atoms are shown in this figure to be displaced from the lattice sites, where like neighbors are closer than the  $(\sqrt{2}a_0)/2$  ( $a_0$ =lattice parameter) value for the nearest-neighbor distance in the fcc structure, and the unlike neighbors are displaced to greater distances. The undistorted fcc lattice is what would be measured by XRD.

We propose that the bond dilation of the unlike atom pairs is the consequence of a wave-function interaction. The Fe-Fe interaction is strong and determined by the hybridization of the *d*-shell electron wave functions, whereas the Cu-Cu

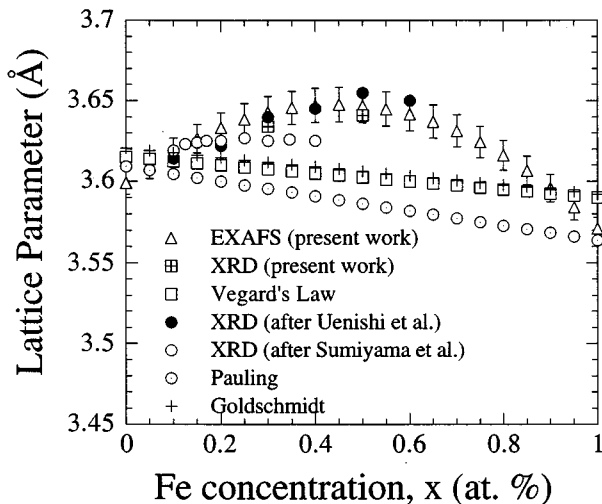


FIG. 11. Plot of lattice parameter versus Fe concentration in Cu-Fe alloys. Values calculated from XRD measurements for the samples studied here are plotted with values calculated using the atomic radii of Goldschmidt and Pauling and values calculated using the atomic radii measured via the EXAFS analysis presented here. Solid line represents Vegard's law. The circles appearing at  $0 \leq x \leq 0.40$  correspond to values measured for vapor-quenched Cu-Fe after Sumiyama, Yoshitake, and Nakamura (Ref. 4), and the solid circles appearing at  $0 \leq x \leq 0.60$  correspond to values measured for HEBM Cu-Fe after Uenishi *et al.* (Ref. 26).

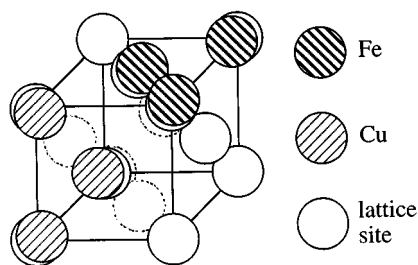


FIG. 12. Schematic representation of atom arrangements which are consistent with the EXAFS modeling results (the drawing is not drawn to relative scale). The solid circles represent lattice sites in an ideal fcc structure with dashed circles representing the background plane of atoms. The hashed circles are the atoms displaced from the ideal lattice indicating the dilation of the unlike atom bonds and the affinity for like pairing. For clarity not all lattice sites are filled.

neighbors experience strong interaction by the overlap of the *s*-shell electron wave functions and the hybridization of the inner *p* and *d* shells. However, the dilated bonds measured between Cu and Fe indicate either a very weak interaction or a repulsion exist between unlike neighbors. Pearson suggests that bond dilation observed in solid solutions may occur when repulsive forces are generated by the overlap of the tails of the electron wave functions.<sup>57</sup> However, because the magnetic moment of Fe is largely unaffected by the introduction of Cu there is little or no hybridization of the Fe *d* shell by the Cu 4*s*, 3*p* or 3*d* electrons. We propose that the strong interaction between the like atom pairs provide Coulombic forces which establish geometrical limitations which prohibit the Fe-Cu pairs from coming any closer than the measured distances.

## V. CONCLUSIONS

We have performed x-ray diffraction (XRD) and extended x-ray-absorption fine structure (EXAFS) measurements, including EXAFS near-neighbor modeling analyses on Cu<sub>50</sub>Fe<sub>50</sub> and Cu<sub>70</sub>Fe<sub>30</sub> high-energy ball-milled (HEBM) samples, to investigate the effects of HEBM on the local structure and chemistry of samples having a positive heat of mixing.

(1) X-ray-diffraction measurements for both HEBM samples illustrate only one family of fcc diffraction peaks suggesting that the Fe and Cu coexists in a single fcc phase. Lattice parameters of 3.641 and 3.634 Å were calculated for the Cu<sub>50</sub>Fe<sub>50</sub> and Cu<sub>70</sub>Fe<sub>30</sub> samples, respectively. These values are significantly greater than that of fcc Cu, 3.615 Å, representing a 2.1 and 1.6 % increase in unit-cell volume, respectively, and are larger still compared with the values predicted by Vegard's law (3.6025 Å for Cu<sub>50</sub>Fe<sub>50</sub>, a change of 3.24% in volume, and 3.6075 Å for Cu<sub>70</sub>Fe<sub>30</sub>, a change of 2.22% in volume). Lattice expansions of similar magnitude have been measured in other HEBM Cu-Fe samples.<sup>26</sup> Vapor-quenched Cu-Fe films have been measured to have much smaller lattice expansions.<sup>4,5</sup>

(2) Fourier-transformed Fe and Cu EXAFS data illustrate that both the Fe and Cu atoms reside in a close-packed arrangement similar to that of fcc Cu. A shift in the nearest-neighbor peak position to higher *r* values in the HEBM samples compared with that of the fcc Cu standard, suggests that the lattice positions for Cu and Fe are slightly expanded

with respect to Cu. This is in qualitative agreement with the XRD-measured lattice expansion.

(3) Fitting of the nearest-neighbor peak region in the Fourier-transformed EXAFS data was performed with parametrized theoretical EXAFS data generated via the FEFF 3.11 codes.<sup>44</sup> Best fits to the first coordination sphere were obtained using two shells of atoms, one of Cu and the other of Fe, displaced from one another. Results indicate that the nearest-neighbor chemistry of the HEBM samples are very close to that of the nominal stoichiometry of the starting materials indicating that atomic-level mixing has occurred and a supersaturated-solid-solution exist.

(4) From the EXAFS fitting analysis the nearest-neighbor bond distances for like and unlike neighbors were deduced. Bond distances between like neighbors are very close to those one would expect for elemental fcc phases of these elements. However, the unlike atom pairs are calculated to be dilated to a distance of  $2.625 \pm 0.01$  Å. Lattice parameters calculated using the bond distances determined from EXAFS are found to be in excellent agreement with those measured via XRD.

(5) The atomic radii deduced from EXAFS modeling are compared with those determined from XRD measurements and those calculated using Goldschmidt and Pauling radii. The EXAFS radii corresponding to like atom pairs are in excellent agreement with the values from XRD, Goldschmidt and Pauling. However, the unlike atom pair bond distances are much greater than the sum of these radii. A qualitative model is proposed that attributes this effect to a Coulombic displacement of unlike pairs caused by the affinity for like pair bonding. This affinity originates from the hybridization of the valence electron wave functions, acts to define a minimum interatomic distance between like pairs in the fcc structure, and displaces the unlike pairs, which have a lower binding energy, away from one another.

These results establish that atomic-level mixing has indeed occurred around Fe and Cu sites in these HEBM Cu-Fe samples. Although researchers have long assumed that HEBM facilitates the formation of alloys through solid-state transformations, often using the disappearance of the Bragg reflections in diffraction experiments as evidence, this represents direct experimental evidence obtained via an element-specific, local probe having sufficient sensitivity to investigate the chemistry of the first coordination sphere.

## ACKNOWLEDGMENTS

The authors express their appreciation to Dr. Kristl Hathaway (NRL) for valuable discussions concerning the magnetic and electronic properties of the Fe-Cu and Fe/Cu systems, and to Professor J. J. Rehr and associates (University of Washington) for providing us with the theoretical EXAFS simulation (i.e., FEFF) codes used here. This research was carried out in part at the National Synchrotron Light Source (Brookhaven National Laboratories, Upton, New York), which is sponsored by the U.S. Department of Energy. In addition, some of the samples included in this research were processed and characterized with support from the Spanish CICYT through projects Mat. 92-0491 and Mat. 92-0404. A.H. acknowledges support to the BBV Foundation and K.M.K. acknowledges support of the National Research Council during the time of this research.

- <sup>1</sup>J. Q. Xiao, J. S. Jiang, and C. L. Chien, *Phys. Rev. Lett.* **68**, 3749 (1992).
- <sup>2</sup>A. E. Berkowitz, J. R. Mitchel, M. J. Carey, A. P. Young, S. Zhang, F. E. Spada, F. T. Parker, A. Hutten, and G. Thomas, *Phys. Rev. Lett.* **68**, 3745 (1992).
- <sup>3</sup>M. Hansen, in *Constitution of Binary Alloys*, edited by M. Hansen (McGraw-Hill, New York, 1958), p. 580.
- <sup>4</sup>K. Sumiyama, T. Yoshitake, and Y. Nakamura, *J. Phys. Soc. Jpn.* **53**, 3160 (1984).
- <sup>5</sup>C. L. Chien, S. H. Liou, D. Kofalt, W. Yu, T. Egami, and T. R. McGuire, *Phys. Rev. B* **33**, 3247 (1986).
- <sup>6</sup>A. Y. Yermakov, Y. Y. Yurchikov, and V. A. Varinov, *Phys. Met. Metallogr.* **52**, 50 (1981).
- <sup>7</sup>C. C. Koch, O. B. Gavin, C. G. Mackamey, and J. O. Scarbrough, *Appl. Phys. Lett.* **43**, 1017 (1983).
- <sup>8</sup>T. Nasu, C. C. Koch, K. Nagaoka, N. Itoh, M. Sakurai, and K. Suzuki, *Mater. Sci. Eng. A* **134**, 1385 (1991).
- <sup>9</sup>H. Miura, S. Isa, and K. Omuro, *Jpn. J. Appl. Phys.* **29**, L339 (1990).
- <sup>10</sup>T. Nasu, K. Nagaoka, N. Itoh, and K. Suzuki, *J. Non-Cryst. Solids* **122**, 216 (1990).
- <sup>11</sup>E. Gaffet and M. Harmelin, *J. Less Common Met.* **157**, 201 (1990).
- <sup>12</sup>A. R. Yavari and P. J. Desre, *Phys. Rev. Lett.* **65**, 2571 (1990).
- <sup>13</sup>R. Shulz, M. Trudeau, and J. Y. Huot, *Phys. Rev. Lett.* **62**, 2849 (1989).
- <sup>14</sup>M. L. Trudeau, R. Shulz, D. Dussault, and A. V. Neste, *Phys. Rev. Lett.* **64**, 99 (1990).
- <sup>15</sup>A. R. Yavari, P. J. Desre, and T. Benamer, *Phys. Rev. Lett.* **68**, 2235 (1992).
- <sup>16</sup>P. H. Shingu, K. N. Ishihara, K. Uenishi, J. Koyama, B. Huang, and S. Nasu, in *Solid State Powder Processing*, edited by A. H. Clauer and J. J. de Barbadillo (Minerals, Metals and Materials Society, Warrendale, PA, 1990), pp. 21–24.
- <sup>17</sup>J. Kuyama, H. Inui, S. Imaoka, K. N. Ishihara, and P. Shingu, *Jpn. J. Appl. Phys.* **30**, L854 (1991).
- <sup>18</sup>K. Uenishi, K. F. Kobayashi, K. N. Ishihara, and P. H. Shingu, *Mater. Sci. Eng. A* **134**, 1342 (1991).
- <sup>19</sup>V. G. Harris, W. T. Elam, B. N. Das, and N. C. Koon, National Synchrotron Light Source Report No. BNL52415, B-193 (1993).
- <sup>20</sup>P. Crespo, A. Hernando, A. G. Escorial, K. M. Kemner, and V. G. Harris, *J. Appl. Phys.* **76**, 6322 (1994).
- <sup>21</sup>P. J. Schilling, J.-H. He, J. Cheng, and E. Ma, *Appl. Phys. Lett.* **68**, 767 (1996).
- <sup>22</sup>P. S. Jilman and J. S. Benjamin, *Annu. Rev. Mater. Sci.* **13**, 279 (1983).
- <sup>23</sup>R. B. Schartz, R. R. Petrich, and C. K. Saw, *J. Non-Cryst. Solids* **76**, 281 (1985).
- <sup>24</sup>A. Hernando, P. Crespo, A. G. Escorial, and J. M. Barandiaran, *Phys. Rev. Lett.* **70**, 3521 (1993).
- <sup>25</sup>P. Crespo, A. Hernando, A. R. Yavari, O. Drbohlav, A. G. Escorial, J. M. Barandiaran, and I. Orue, *Phys. Rev. B* **48**, 7134 (1993).
- <sup>26</sup>K. Uenishi, K. F. Kobayashi, S. Nasu, H. Hatano, K. N. Ishihara, and P. H. Shingu, *Z. Metallkd.* **83**, 132 (1992).
- <sup>27</sup>R. M. Bozorth, *Ferromagnetism* (Van Nostrand, Princeton, NJ, 1978).
- <sup>28</sup>J. T. Norton, *Trans. Metall. Soc. AIME* **116**, 386 (1935).
- <sup>29</sup>L. S. Darken and H. A. Wriedt, *Trans. Metall. Soc. AIME* **218**, 30 (1960).
- <sup>30</sup>J. W. Klement, *Trans. Metall. Soc. AIME* **233**, 1180 (1965).
- <sup>31</sup>E. F. Kneller, *J. Appl. Phys.* **35**, 2210 (1964).
- <sup>32</sup>T. Ambrose, A. Gavrin, and C. L. Chien, *J. Magn. Magn. Mater.* **124**, 15 (1993).
- <sup>33</sup>P. H. Shingu, K. N. Ishihara, K. Uenishi, J. Kuyama, B. Huang, and S. Nasu, in *Solid State Powder Processing* (Ref. 16), p. 21.
- <sup>34</sup>L. Pauling, in *Theory of Alloy Phases* (American Society for Metals, Cleveland, OH, 1956), p. 220.
- <sup>35</sup>E. C. Stoner, *Philos. Mag.* **15**, 1018 (1933).
- <sup>36</sup>B. Cordts, D. M. Pease, and L. V. Azaroff, *Phys. Rev. B* **22**, 4692 (1980).
- <sup>37</sup>D. M. Pease, G. H. Hayes, M. Choi, J. I. Budnick, W. A. Hines, R. Hesagawa, and S. M. Heald, *J. Non-Cryst. Solids* **61-62**, 1359 (1984).
- <sup>38</sup>M. Munoz, P. J. Durham, and B. L. Gyorffy, *J. Phys. F* **12**, 1497 (1982).
- <sup>39</sup>V. L. Moruzzi, J. F. Janak, and A. R. Williams, *Calculated Electronic Properties of Metals* (Pergamon, New York, 1978).
- <sup>40</sup>C. L. Fu and A. J. Freeman, *Phys. Rev. B* **35**, 925 (1987).
- <sup>41</sup>E. Wimmer, H. Krakauer, M. Weinert, and A. J. Freeman, *Phys. Rev. B* **24**, 864 (1981).
- <sup>42</sup>Brand names are used here to be specific. Their use is not to be interpreted as an endorsement by the Federal government.
- <sup>43</sup>D. E. Sayers and B. A. Bunker, in *X-ray Absorption: Principles, Applications, Techniques of EXAFS, SEXAFS and XANES*, edited by D. C. Koningsberger and R. Prins (Wiley, New York, 1988), p. 211.
- <sup>44</sup>J. J. Rehr, J. M. d. Leon, S. I. Zabinsky, and R. C. Albers, *J. Am. Chem. Soc.* **113**, 5135 (1991).
- <sup>45</sup>E. Stern, D. Sayers, and F. Lytle, in *X-ray Absorption Fine Structure*, edited by S. S. Hasnain (Harwood, Chichester, UK, 1991), p. 751.
- <sup>46</sup>P. H. Duwez, R. H. Willens, and W. Klement, *J. Appl. Phys.* **31**, 1136 (1960).
- <sup>47</sup>J. B. Newkirk, *Trans. Metall. Soc. AIME* **138**, 1214 (1957).
- <sup>48</sup>A. N. Mansour, C.-P. Wong, and R. A. Brizzolara, *Phys. Rev. B* **50**, 12 401 (1994).
- <sup>49</sup>G. E. Ice, C. J. Sparks, A. Habenschuss, and L. B. Shaffer, *Phys. Rev. Lett.* **68**, 863 (1992).
- <sup>50</sup>L. Reinhard, J. L. Robertson, S. C. Moss, G. E. Ice, P. Zschick, and C. J. Sparks, *Phys. Rev. B* **45**, 2662 (1992).
- <sup>51</sup>B. Schonfeld, G. E. Ice, C. J. Sparks, H.-G. Haubold, W. Scheika, and L. B. Shaffer, *Phys. Rev. B* **183**, 79 (1994).
- <sup>52</sup>V. M. Goldschmidt, *Z. Phys. Chem. (Leipzig)* **133**, 397 (1928).
- <sup>53</sup>L. Pauling, *The Nature of the Chemical Bond* (Cornell University Press, Ithaca, 1940).
- <sup>54</sup>L. Pauling, *J. Am. Chem. Soc.* **69**, 542 (1947).
- <sup>55</sup>L. Pauling, *Proc. R. Soc. London* **196A**, 343 (1949).
- <sup>56</sup>L. Pauling, *Phys. Rev.* **54**, 899 (1938).
- <sup>57</sup>W. B. Pearson, in *The Chemical Structure of Solids, Vol. I*, edited by N. B. Hannay (Plenum, New York, 1976), Vol. 1, p. 115.